Measurement report: Assessment of Asian emissions of ethane, propane, carbon monoxide, and NO$_x$ based on observations from the island of Hateruma

Adedayo R. Adedeji[1], Stephen J. Andrews[1], Matthew J. Rowlinson[1,2], Mathew J. Evans[1,2], Alastair C. Lewis[1,2], Shigeru Hashimoto[3], Hitoshi Mukai[3], Hiroshi Tanimoto[3], Yasunori Tohjima[3], and Takuya Saito[3]

[1]Wolfson Atmospheric Chemistry Laboratories, Department of Chemistry, University of York, York, UK
[2]National Centre for Atmospheric Science, Department of Chemistry, University of York, York, UK
[3]National Institute for Environmental Studies, 16-2 Onogawa, Tsukuba, Ibaraki 305-8506, Japan

Correspondence: Adedayo R. Adedeji (adedayo.adedeji@york.ac.uk)

Abstract. The island of Hateruma is the southernmost inhabited island of Japan. Here we interpret observations of carbon monoxide (CO), ethane (C$_2$H$_6$), propane (C$_3$H$_8$), nitrogen oxides (NO$_x$ and NO$_y$) and ozone (O$_3$) made from the island in 2018 with the GEOS-Chem atmospheric chemistry transport model. We simulated the concentrations of these species within a nested grid centered over the site, with a model resolution of 0.5°×0.625°. We use the Community Emissions Data System (CEDS) emissions dataset for anthropogenic emissions and add a geological source of C$_2$H$_6$ and C$_3$H$_8$. The model captured the seasonality of primary pollutants (CO, C$_2$H$_6$, C$_3$H$_8$) at the site - high concentrations in the winter months when oxidation rates are low and flow is from the north, and low concentrations in the summer months when oxidation rates are higher and flow is from the south. It also simulates many of the synoptic scale events with Pearson's correlation coefficients (r) of 0.74, 0.88 and 0.89 for CO, C$_2$H$_6$ and C$_3$H$_8$, respectively. Concentrations of CO are well simulated by the model (with a gradient of best fit between model and measurements of 0.91) but simulated concentrations of C$_2$H$_6$ and C$_3$H$_8$ are significantly lower than the observations (gradients of best fit between model and measurement of 0.57 and 0.41, respectively), most noticeably in the winter months. Simulated NO$_x$ concentrations were underestimated but NO$_y$ appear to be overestimated. The concentration of O$_3$ is moderately well simulated (gradient of best fit line of 0.76, with an r of 0.87) but there is a tendency to underestimate concentrations in the winter months. By switching off the model's biomass burning emissions we show that during winter biomass burning has limited influence on the concentration of compounds in the winter but can represent a sizeable fraction in the summer. We also show that increasing the anthropogenic emissions of C$_2$H$_6$ and C$_3$H$_8$ in Asia by factors of 2.22 and 3.17, respectively, significantly increases the model's ability to simulate these species in the winter months, consistent with previous studies.

1 Introduction

Without good quality, long-term measurements of volatile organic compounds (VOCs) and other ozone precursors, it is impossible to identify the key contributors to ozone formation, understand trans-boundary pollution and validate emissions invento-

ries. It is important to have these observations both on urban scales where they can inform local conclusions, but also in more background sites which are exposed to regional scale pollution.

Hateruma is the southernmost inhabited island in the Japanese archipelago. It is situated off the coast of Taiwan (Figure 1) in
25   the Pacific ocean. It is 500 km southwest and 250 km east of Okinawa Island and Taiwan respectively (Yokouchi et al., 2011). As a part of its global monitoring effort, the Japanese National Institute for Environmental Studies' (NIES) Centre for Global Environmental Reseach (CGER) operates an observation station at Hateruma to carry out atmospheric measurements and it has made measurements of atmospheric constituents over a number of years. Saito et al. (2010) continuously measured the atmospheric mixing ratios of perfluorocarbons (PFCs) at Hateruma Island and Cape Ochiishi since 2006, to infer their global
30   and regional emissions. Tohjima et al. (2020) used observed variabilities in CO_2 (ΔCO_2) and methane (ΔCH_4) between 1997 and 2020 to show a traceable CO_2 emission reduction in China during the COVID-19 pandemic between February and March 2020.
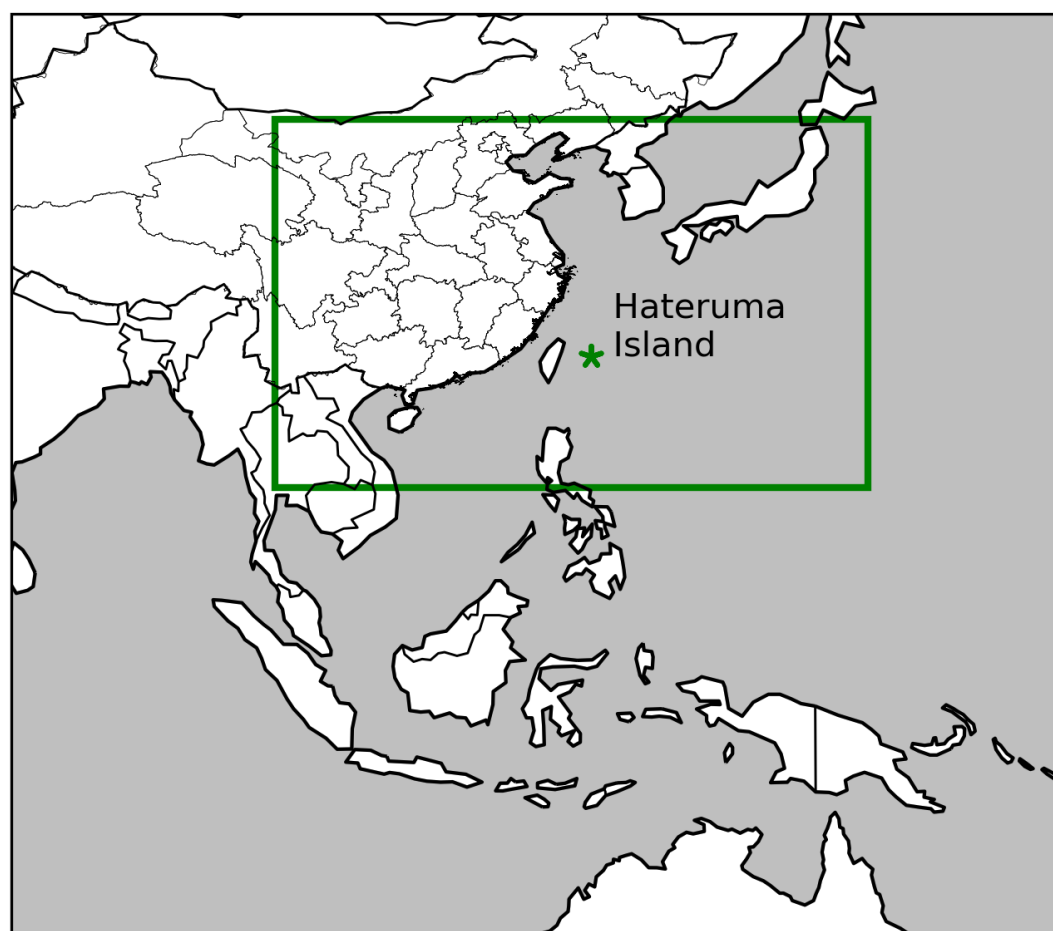
Figure 1. Location of the island of Hateruma (indicated by the star) and the region of the high resolution modelling domain (indicated by the green box)

Over the course of a year, the observatory is exposed to air masses from a wide range of locations. We calculate ten day back trajectories for the site every hour from January to December in 2018 (52 weeks duration) using meteorological data from NCEP Global Forecast System (National Centers for Environmental Prediction, National Weather Service, NOAA, U.S. Department of Commerce, 2015) and the FLEXible PARTicle dispersion model (FLEXPART) (Stohl et al., 2003, 2005). Figure 2 (right) shows the ratio of the time that these ten day trajectories spent over the different regions shown in Figure 2 (left). Over the year, most of the air is oceanic in origin from either the Northern or Southern Pacific (43% and 34%). However the air masses can also spend a significant fraction of the time over Inland China (3.6%), Russia (4.6%), Korea (1.7%), Japan, (3.9%), South East Asia (3.1%), the Philippines (1.2%) and the three East China city regions (3.7%).
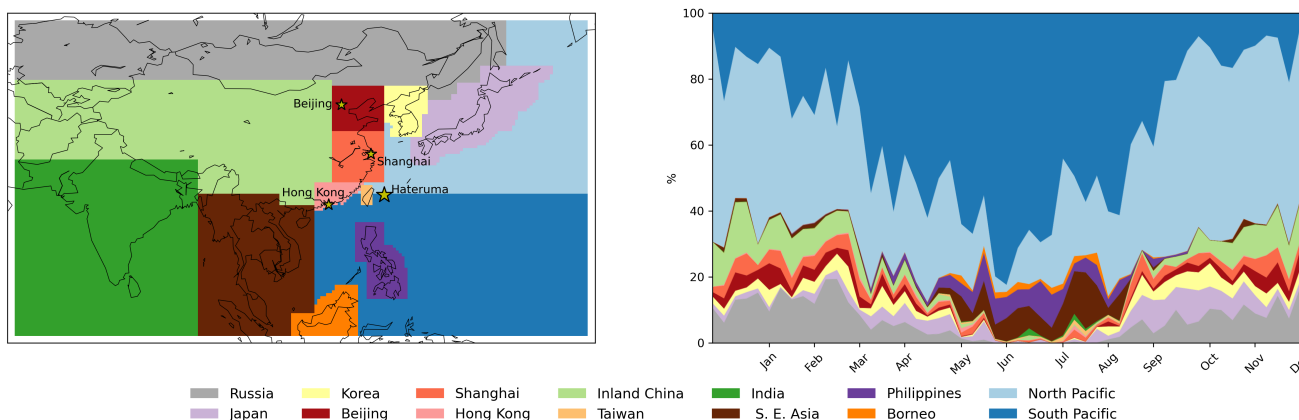
Figure 2. Trajectory analysis of air arriving at Hateruma; (left) location of the regions analysed; (right) weekly average percentage of time air masses spent over these regions

There is a significant seasonal variation in air mass origin. The fraction that is oceanic remains roughly the same (around 60% in the winter and 70% in the summer) over a year but the origin changes between mainly northern Pacific in the winter months to southern Pacific in the summer. This pattern can be attributed to the annual meteorological cycle of this region characterised by the East Asian monsoon seasons (Shirai et al., 2010; Yokouchi et al., 2006, 2011, 2017). For the remaining 30% -40% of the time, flow from China, Japan, Korea and Russia dominates in the winter, spring and autumn. During the summer months, the air originates from a southerly direction (Philippines, South East Asia, Borneo).

The site is therefore subject to air from a large number of locations within Asia. Here we use a chemical transport model (GEOS-Chem) to understand the processes controlling the concentrations of key atmospheric gases (CO, C_2H_6, C_3H_8, NO, NO_2, NO_y, and O_3) measured at the site. We start with a description of the observations (Section 2.1) and the model configuration (Section 2.2). We then provide a general evaluation of the model performance in Section 3. In Section 3.1 we present the performance of the model in simulating the meteorological variables. In Sections 3.2 to 3.7 we evaluate the model's ability to simulate the concentrations of the measured gases. Section 4 assesses the sensitivity of the model to biomass burning emissions

and in Section 5 we explore scaling anthropogenic Asian C_2H_6 and C_3H_8 emissions to better reflect the observations at the site. We draw conclusions in Section 6.

2 Observations and model setup

2.1 Observations

The observatory is located on the easterly corner of the island, with a disused airport and the populated area (with electricity generation) located to the west. A number of different observations are made at the site but we are only concerned with a subset of the observations in this study. Table 1 gives the observations used in the study and the method used to make them. Observations are available hourly for most of 2018 with some missing periods.

Table 1. Physical and Chemical variables measured at Hateruma

Compound	Method	Reference
Temperature	Pt100 (YOKOGAWA E734)	-
Wind speed	Wind speed and direction transmitter (YOKOGAWA WA7601)	Shirai et al. (2010)
Wind direction	Wind speed and direction transmitter (YOKOGAWA WA7601)	Shirai et al. (2010)
Relative humidity	Capacitance hygrometer (VISALA HUMICAP HMP155)	-
Carbon Monoxide (CO)	GC/RGD (Peak Performer 2, Peak Laboratories)	Tohjima et al. (2014)
Ethane (C_2H_6)	Preconcentration/GC/MS	Yokouchi et al. (2006); Saito et al. (2010)
Propane (C_3H_8)	Preconcentration/GC/MS	Yokouchi et al. (2006); Saito et al. (2010)
Nitrogen oxide (NO)	$NO/NO_2/NO_y$ analyzer (HSS-100, Sonoma Technology Inc.)	-
Nitrogen dioxide (NO_2)	$NO/NO_2/NO_y$ analyzer (HSS-100, Sonoma Technology Inc.)	-
Nitrogen dioxide (NO_y)	$NO/NO_2/NO_y$ analyzer (HSS-100, Sonoma Technology Inc.)	-
Ozone (O_3)	UV absorption O_3 analyzer (Model 1100, Dylec Inc.)	-

Measurements of CO, ethane, and propane were made with outside air drawn from a main tower (sampling inlet: 36.5 m above ground and 46.5 m above sea level). CO was measured with a gas chromatograph/reduction gas detector (GC/RGD; Peak Performer 2, Peak Laboratories) (Tohjima et al., 2014). Ethane and propane were measured with an automated preconcentration/gas chromatography/mass spectrometry (GC/MS) instrument (7890B/5977B, Agilent Technologies) designed for hourly measurements of natural and anthropogenic halocarbons (Yokouchi et al., 2006; Saito et al., 2010). Ethane and propane measurements were calibrated using a gravimetrically prepared standard gas (Taiyo Nippon Sanso Co. Ltd.).

Air for $NO/NO_2/NO_y$ and O_3 measurements were drawn from a sub tower (sampling inlet: 14.8 m above ground and 24.8 m above sea level). Measurements of NO, NO_2, and NO_y were made by HSS-100 (Sonoma Technology Inc. (STI)) with a blue light converter for NO_2 (NO_x converter) and a molybdenum converter for NO_y (NO_y converter) (Galbally, 2020). The conversion efficiencies of the converters were daily monitored with NO_2 gas ($\approx$5 ppb) generated by a gas dilution system

with gas phase titration (NO_x: 79±3%, NO_y: 98±1%). Detection limit of the NO measurement was about 2 ppt in 1 minute acquisition. Ozone concentration was observed by UV absorption method with an ozone monitor (Dylec 1100, Dylec Co., Ltd), which was calibrated with Standard Reference Photometer No. 35 (National Institute for Standard and Technology) located at NIES.

2.2 Model configuration

75

We use GEOS-Chem Version 12.7.1 which was first described by Bey et al. (2001) (www.geos-chem.org). We use a regional simulation at $0.5° \times 0.625°$ spatial resolution with the domain shown in Figure 1. The model includes detailed HO_x–NO_x–VOC -ozone–halogen–aerosol tropospheric chemistry as described by Sherwen et al. (2016) and is driven by offline meteorology from the NASA Global Modelling and Assimilation Office (http://gmao.gsfc.nasa.gov, last access: 05 September 2021) forward
80 processing product (GEOS-FP).

To generate restart files and boundary conditions, the model was run in a global configuration at $4° \times 5°$ horizontal resolution for two years (1st January 2017 - 1st January 2019) with the first year considered as spin up. We then run the model in its regional configuration using the boundary conditions derived from the global simulation. Figures A1 - A4 in the Appendix shows comparison between the model simulations run at the native meteorological resolution of $0.25° \times 0.3125°$ and the simulation
85 run at $0.5° \times 0.625°$. The differences between the two models are minimal, so we adopt the coarser $0.5° \times 0.625°$ resolution version as it is substantially faster to run with only a small degradation in performance.

We run the model in a slightly different emission configuration than its default. We use the CEDS emissions (Hoesly et al., 2018), with applied monthly and diurnal scale factor, for all anthropogenic emissions, other than for those from aircraft where we use the Aviation Emissions Inventory Code (AEIC) emissions (Stettler et al., 2011). This contrasts with the model default
90 configuration which uses Tzompa-Sosa et al. (2017) and Xiao et al. (2008) for anthropogenic ethane and propane emissions, but does makes our simulation consistent with recent CMIP model evaluations (Griffiths et al., 2021).

We also include geological emissions of ethane and propane that may represent a missing source (Etiope et al., 2019; Dalsøren et al., 2018). We assume a global total of 3.0 Tg year^{-1} of ethane and 1.7 Tg year^{-1} of propane (Dalsøren et al., 2018). We spatially distribute these emissions using a geological methane emission dataset (Etiope et al., 2018).

95 Other emissions include offline soil NO_x (Weng et al., 2020) and online lightning NO_x emissions (Murray et al., 2012). The PARANOX ship plume model by Holmes et al. (2014) which calculates the aging of emissions in ship exhaust plumes for NO_x, HNO_3 and O_3 was applied to the CEDS shipping emissions (Hoesly et al., 2018). Biomass burning emissions uses the Global Fire Emissions Database GFED 4.1 (Andreae and Merlet, 2001; Akagi et al., 2011; Giglio et al., 2013; Randerson et al., 2012; van der Werf et al., 2017). Biogenic emissions follow the estimation from the Model of Emissions of Gases and
100 Aerosols from Nature (MEGAN) 2.1 (Guenther et al., 2012). The natural emissions of acetaldehyde follow the calculation from Millet et al. (2010). Natural sources of NH_3 are adapted from Global Emission InitiAtive (GEIA) with the inclusion of the arctic seabird emissions (Riddick, 2012).

3 Model performance

We now compare the performance of the model, first against the meteorological observations made at the site and then against

105   measurements of atmospheric chemical constituents. We use a number of standard metrics for describing the measurements and model (mean, median, standard deviation, 25th and 75th percentiles). When assessing the model performance we assess this in terms of the Root Mean Square Error (RMSE), mean bias and Pearson's correlation coefficient (r). We also calculate the slope of the best-fit lines using Orthogonal Distance Regression (ODR).

      In the case of wind direction, which is circular not linear, the methodology for the estimation of RMSE and Bias follows Fer-

110   reira et al. (2008) and Carvalho et al. (2012).

3.1 Meteorological variables

Figure 3 shows a comparison between the observed and modelled timeseries for wind speed, wind direction, temperature and relative humidity at the observatory.

      The wind direction (10 m above surface) is plotted in Figure 3 (top left) as the incidence angle of the wind (North = 0° and

115   360°). The observations are given with a resolution of 22.5° clockwise, which gives them a blocky appearance. Overall, the model captured the observed wind direction well throughout the year with few discrepancies. The modelled wind direction has a low RMSE (6.5°) and a slightly high bias (6.5°). This could be attributed to the meteorological fields used in our simulations or to the resolution of the measurements. The seasonal variability of wind direction is well represented in Figure 3 (top left), with the summertime characterised by winds coming from the south, and the winter having winds from a more northerly

120   direction.

      The modelled wind-speed have a correlation coefficient (r) of 0.90 and a RMSE of 2.17 m/s (top right in Figure 3). However, the wind-speeds are lower in the model (mean of 6.43 +/- 3.12 (1σ) m/s), than in the observations (mean of 7.83 +/- 3.79 (1σ) m/s). Surface temperatures (2 m above surface), show a high degree of correlation (r = 0.92) and a RMSE of 1.75 °C, with the mean observed surface temperature (24.53 +/- 4.27 (1σ) °C) close to that simulated (24.76 +/- 3.67 (1σ) °C). There is,

125   however, significant hourly variation not captured by the model (bottom left in Figure 3), potentially reflecting local heating and cooling at the observatory site.

      The modelled surface relative humidity (RH at 2m above surface, bottom right in Figure 3) is less well captured (r = 0.77; RMSE = 11.26 %), with the modelled mean (73.09 +/- 9.89 (1σ) %) lower than the observed mean (82.00 +/- 10.32 (1σ) %). It is not clear what could be causing this difference other than the local environment aroud the observatory.
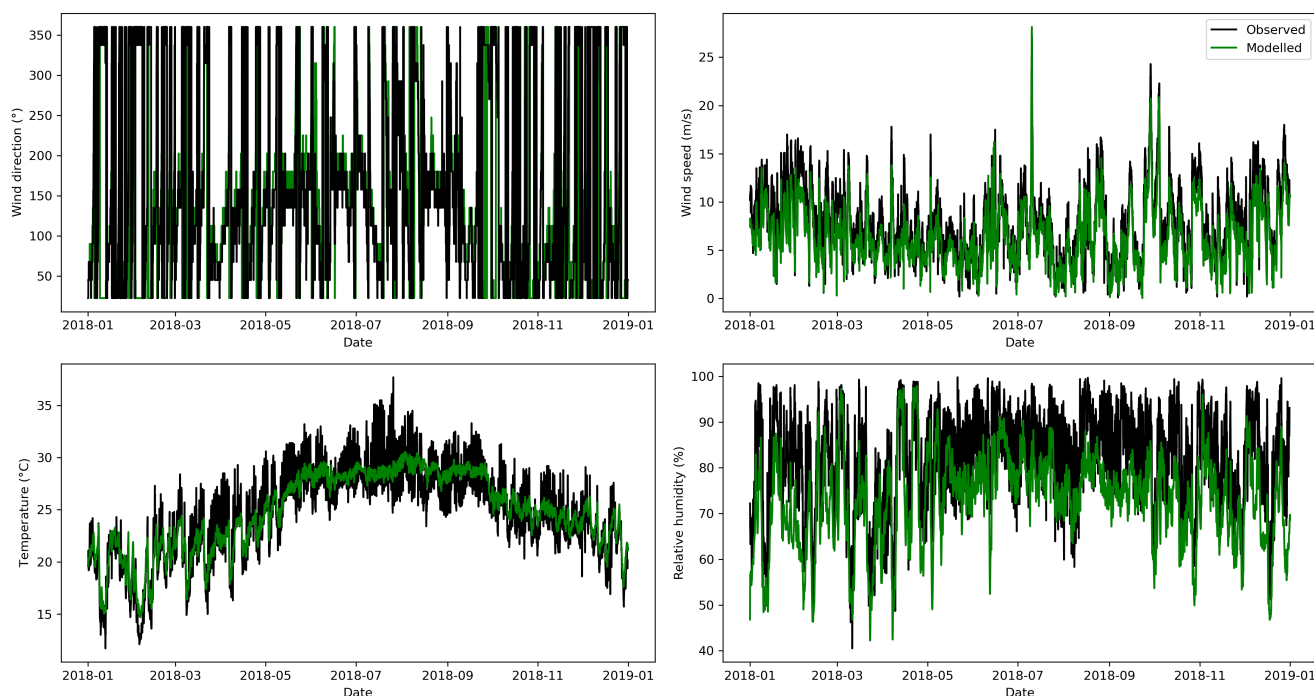
Figure 3. Observed and modelled wind direction (top left), wind speed (top right), temperature (bottom left) and relative humidity (bottom right) at Hateruma

In general, the model performance compared to the meteorological observations is relatively good, reflecting the observational data assimilated into the GEOS-FP meteorological fields. We can now assess the model performance in simulating the concentration of the trace gas concentrations observed at the site.

3.2 Carbon monoxide (CO)

Figure 4 (left) shows the time series of CO measured and modelled at the site, with Figure 4 (right) showing the correlation between the hourly modelled and measured values. Concentrations are highest in the winter months reflecting transport from North Asia (China, Korea, Japan) and the North Pacific (Figure 2), and lower oxidation by OH in the winter months (Schlesinger and Bernhardt, 2020). They are lower in the summer reflecting transport from more southerly regions (further away and typically have lower emissions), and increased oxidation due to enhanced OH concentrations in the summer (Schlesinger and Bernhardt, 2020). Koike et al. (2006) measured CO in northern Japan and reported similar seasonality in CO concentrations over the year.
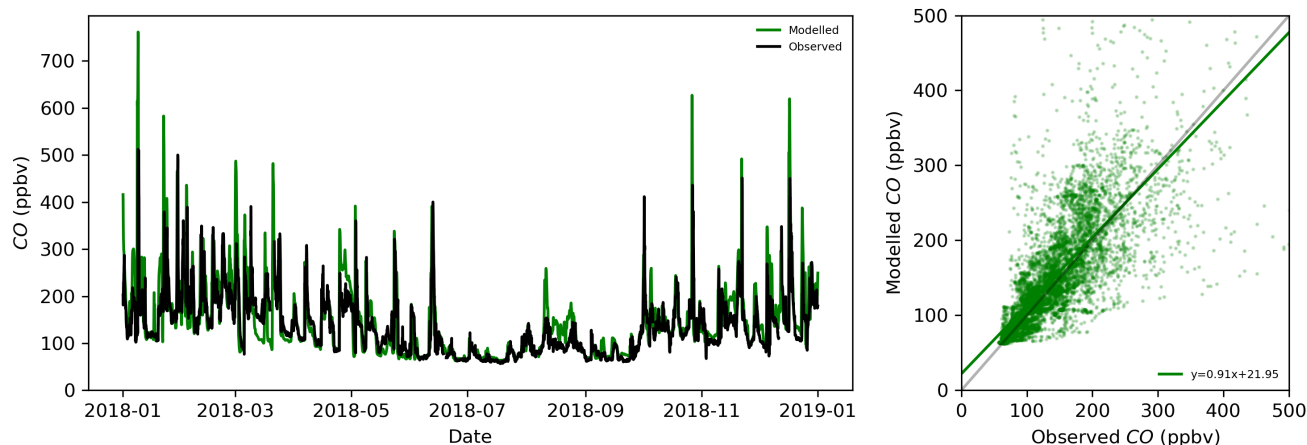
Figure 4. Modelled and measured hourly CO concentrations calculated for Hateruma site

Over the year, the model simulates CO concentration well with a mean value of 146 +/- 77 (1σ) ppbv compared to mean observations of 136 +/- 62 (1σ) ppbv. The median CO concentrations calculated and measured are 127 ppbv and 122 ppbv, respectively. The 25th and 75th percentile modelled is 89 ppbv and 180 ppbv compared to 89 ppbv and 169 ppbv observed. There is a good degree of correlation (r = 0.74) between the model and measurements with a RMSE of 53 ppbv, and the line
145 of best fit having a gradient of 0.91.

3.3 Ethane

Similar to CO, the highest observed ethane (C_2H_6) concentrations occur in the winter with substantially lower concentration occurring in the summer (Figure 5 - left). The model underestimates the mean concentrations (972 +/- 541 (1σ) pptv) compared to the observations (1188 +/- 842 (1σ) pptv)) with a RMSE of 481 pptv. Median concentrations are similarly calculated to be
150 942 pptv, with a 25th to 75th percentile spread of 552-1386 ppbv, while the observations are 1134 pptv with a spread of 368-1825 pptv. This underestimate in modelled ethane is most noticeable in the winter months. However, in the summer the model can overestimate. This leads to two populations in the model - measurement scatter plot (Figure 5 - right). With a strongly correlated but overestimated population at observed concentrations below 500 pptv (in the summer), and another population, with underestimated concentration above this (in winter). The correlation coefficient between the model and measurement is
155 relatively high at 0.88 but the line of best fit between model and measurement is dominated by the wintertime underestimate to give a slope of 0.57.
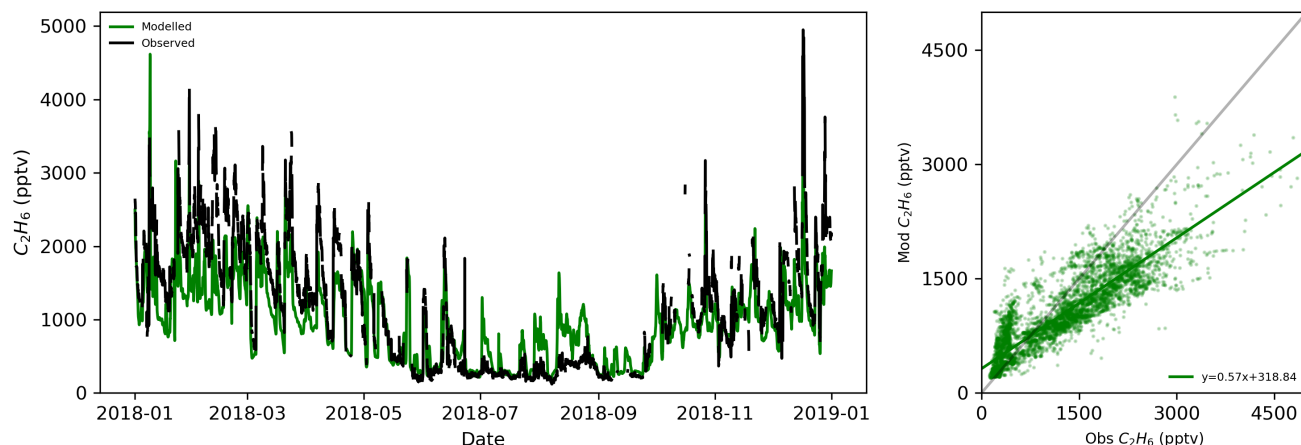
Figure 5. Modelled and measured hourly C_2H_6 concentrations calculated for Hateruma site

3.4 Propane

Figure 6 (left) shows the comparison between the measured and modelled time series for propane (C_3H_8). A similar pattern to C_2H_6 is seen with high winter time concentrations and much lower values in the summer. Unlike C_2H_6 though, a summer time overestimate is not evident. The model captures much of the variability in the C_3H_8 concentration with a correlation coefficient of 0.89 (Figure 6 - right). The mean concentration of C_3H_8 is 391 +/- 432 (1σ) pptv for the measurements and 210 +/- 198 (1σ) pptv for the model. The median C_3H_8 concentration calculated and measured is 156 pptv (5th and 75th percentiles of 69 pptv and 335) and 221 pptv (5th and 75th percentiles of 62 pptv and 611 pptv) respectively. The RMSE is 320 pptv and the gradient of the line of best fit between calculated results and measurements is 0.41. Thus, similar to C_2H_6, the model substantially underestimates C_3H_8 concentrations.
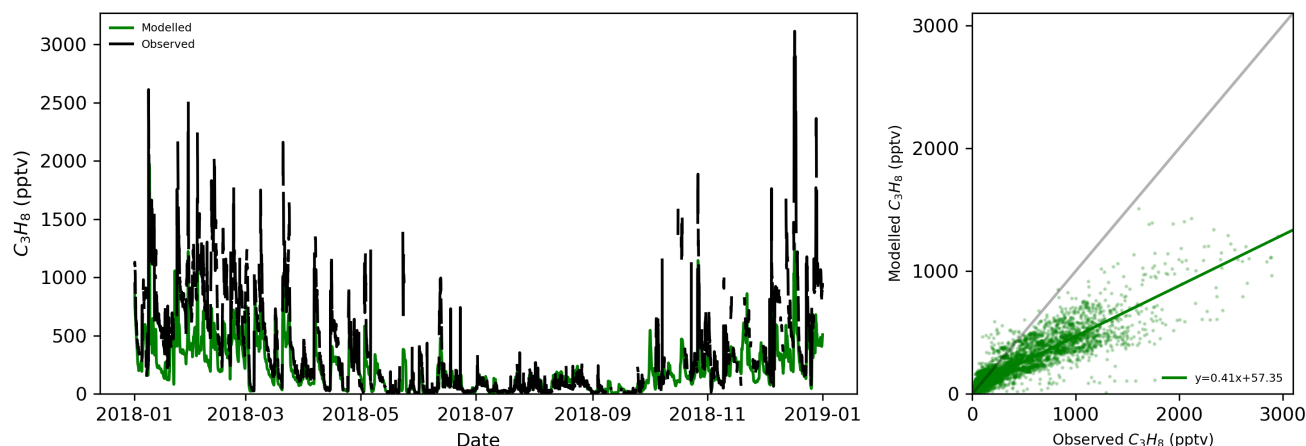
Figure 6. Modelled and measured hourly C_3H_8 concentrations calculated for Hateruma site

3.5 NO$_x$

We evaluate here the model's performance in simulating NO and NO$_2$ (collectively known as NO$_x$). The short lifetime of NO and NO$_2$ (on the order of minutes to hours during the day) makes evaluation against model data difficult due to large and rapid variations. During the day NO concentrations are high due to its photolytic NO$_2$ source, whereas, at night, away from recent emissions, its concentrations are effectively zero. For this evaluation, we compare mean day values (06:00 local to 18:00 local) between the model and observation. Figure 7 shows the comparison between the measured and modelled daytime mean for the NO concentration. The mean observed value (7 +/- 28 (1σ) pptv) is substantially lower than the modelled value (21 +/- 41 (1σ) pptv). The model also shows very little skill in the day to day variability with an r of 0.03 and a gradient of the best fit line of 0.05.
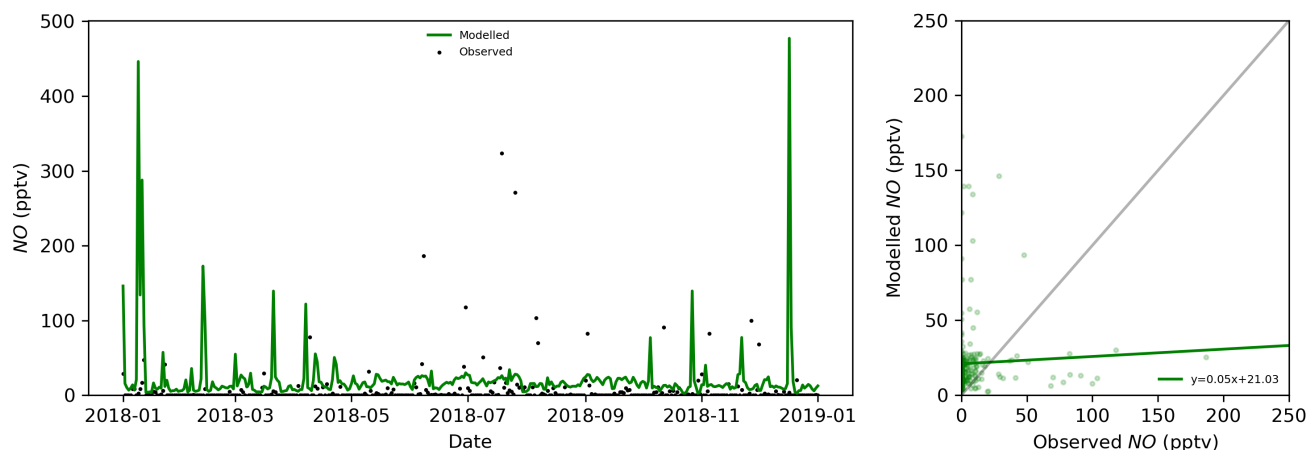
Figure 7. Modelled and measured day mean NO concentrations calculated for Hateruma

Figure 8 (left) compares the time series of daily average NO$_2$ between the measured and modelled, with Figure 8 (right) showing the relationship as a scatter plot and best-fit line. The model simulates NO$_2$ better than NO. The mean NO$_2$ concentration measured is 260 +/- 185 (1σ) pptv while the modelled NO$_2$ mean concentration is 182 +/- 323 (1σ) pptv. The median NO$_2$ concentration observed is 198 pptv with a 25th and 75th percentile range 127 and 335 pptv, whereas that modelled is and 121 pptv, with a 25th to 7th percentile range of 97 pptv and 152 pptv. The correlation coefficient between observation and measurement is though low (0.36) with RMSE of 322 pptv, and a gradient of the best-fit line of 0.65.

Generally, the model performance for the NO$_x$ species is poorer than for other species. This likely reflects a number of problems. It is difficult to make observations at these low concentrations (Reed et al., 2016) and for many days the NO observations are below the detection limit. It also likely reflects the short lifetime of NO$_x$ making it susceptible to local chemical and emissions processes which the model can not resolve. However, in general the modelled NO$_x$ (dominated by NO$_2$) underestimates that observed.
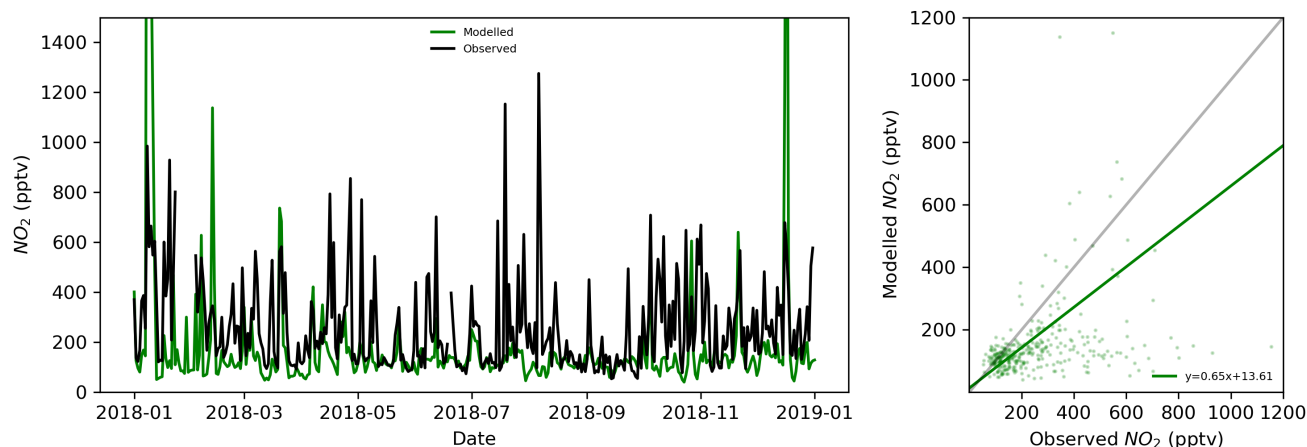
Figure 8. Modelled and measured daily mean NO_2 concentrations calculated for Hateruma

3.6 NO_y

Figure 9 (left) shows the daily average measured and modelled time-series for gas phase reactive nitrogen species (NO_y). We define here NO_y for the model as $NO + NO_2 + 2 \times N_2O_5 + HNO_2 + HNO_3 + PAN$ (which will tend to marginally underestimate the true modelled NO_y). We assumed that none of the particulate nitrate is measured. Figure 9 (right) shows

190 the scatter plot and line of best-fit between measurements and calculations. The mean observed NO_y concentration is 683 +/-698 (1σ) pptv while the mean modelled NO_y concentration is 1173 +/- 1340 (1σ) pptv. The correlation coefficient between observation and model calculations is 0.79 with RMSE of 1035 pptv. The gradient of the best-fit line is 1.55. Thus the model appears to over estimate NO_y concentrations by roughly 50% despite not including some of the NO_y species and the potential for some particulate NO_y being sampled by the observations. The model performance is better than for NO_x. However, whereas

195 the NO_x appears to be underestimated in the model, the NO_y is overestimated.

A simulation without shipping emissions within the high resolution domain, reduces NO_y concentrations by 25%. Thus, even switching off these emissions entirely, would not compensate fully for the model overestimate and would makes the model underestimation of NO_x worse. It is therefore unclear why the model overestimates the NO_y concentrations. This could indicate an excessive emissions in the region, too long a modelled NO_y lifetime, or, some difficulty in the model chemistry

200 Further work will be necessary to understand NO_x and NO_y in the region.
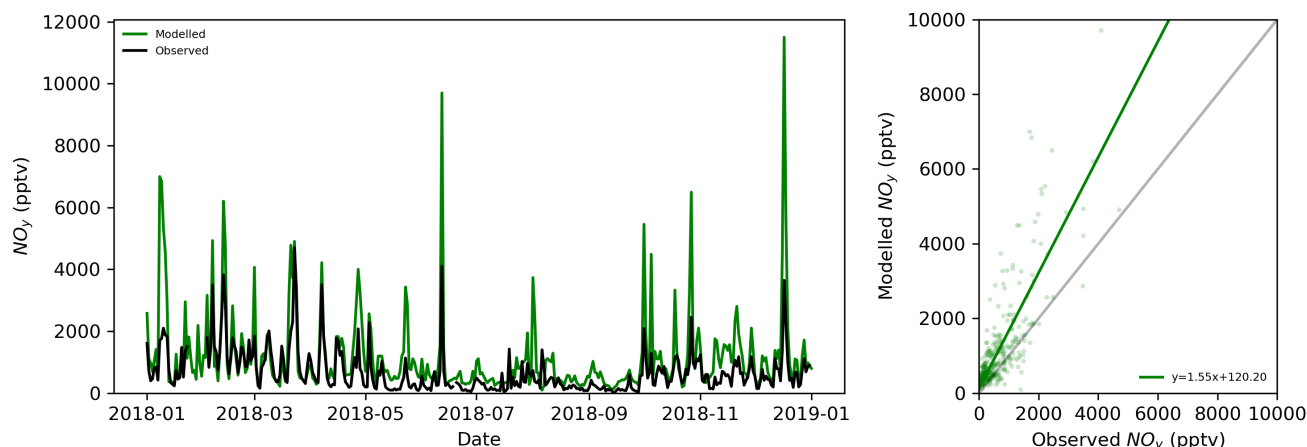
Figure 9. Modelled and measured daily mean NO_y concentrations calculated for Hateruma

3.7 Ozone

Figure 10 (left) shows the measured and modelled timeseries for O_3. In general, the model performs well (RMSE of 8 ppbv; mean measured O_3 of 38 +/- 16 (1σ) ppbv; mean model O_3 of 36 +/- 14 (1σ) ppbv) and simulates much of the variability with a correlation coefficient (r) of 0.87. However, the line of best fit between observed and model results is low, with a gradient of 0.76 (Figure 10 - right). The median O_3 concentration calculated is 35 ppbv (25th and 75th percentiles of 22 ppbv and 46 ppbv) and whereas that measurement is 40 ppbv (25th and 7th percentiles of 24 ppbv and 49 ppbv).

During the summer, there are periods of low O_3, reaching 6.5 ppbv. The model fails to capture these low concentrations simulating a minimum of 10 ppbv. Conversely, in the winter months, the model reproduces much of the variability but has a tendency to underestimate the observed concentrations. Overall, this leads to overestimates at the low concentrations and underestimates at the high concentrations, and thus a reduced gradient in the scatter plot (Figure 1
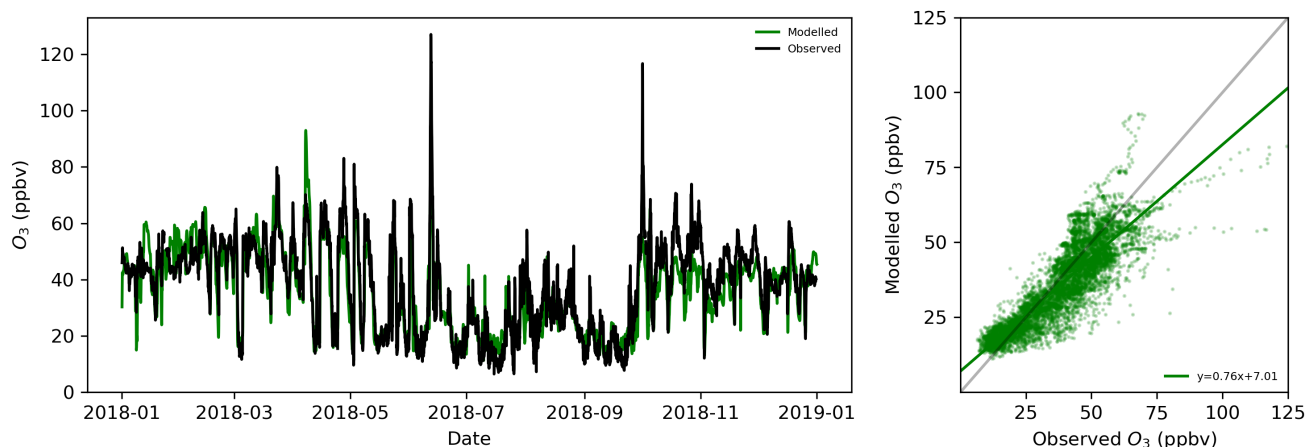
Figure 10. Modelled and measured hourly O_3 concentrations calculated for Hateruma site

3.8 Summary

In general the model has some skill at picking out the variations in meteorological history of the air masses arriving at the site, reflected in the generally high correlation coefficients between the model and the measurements. This mainly reflects the quality of the meteorological fields used. The success in simulating the absolute concentrations is more varied. Table 2 summarizes the

215 mean model and measured concentrations for spring (February-April), summer (May-July), autumn (August-October), winter (November-January).

Table 2. Mean and standard deviations in concentrations of measured and modelled species over different seasons

	Spring		Summer		Autumn		Winter	
	Measured	Modelled	Measured	Modelled	Measured	Modelled	Measured	Modelled
CO (ppbv)	177 +/- 56	178 +/- 73	99 +/- 49	100 +/- 54	110 +/- 45	120 +/- 51	160 +/- 61	187 +/- 85
C_2H_6 (pptv)	1854 +/- 611	1382 +/- 441	458 +/- 415	554 +/- 366	579 +/- 476	698 +/- 359	1638 +/- 691	1249 +/- 468
C_3H_8 (pptv)	588 +/- 416	314 +/- 195	105 +/- 187	79 +/- 86	154 +/- 242	118 +/- 117	646 +/- 473	332 +/- 212
NO (pptv)	3 +/- 9	20 +/- 28	16 +/- 49	19 +/- 6	6 +/- 18	17 +/- 16	6 +/- 17	30 +/- 74
NO_2 (pptv)	276 +/- 160	169 +/- 166	222 +/- 178	132 +/- 42	229 +/- 190	123 +/- 74	316 +/- 193	296 +/- 602
NO_y (pptv)	1183 +/- 882	1497 +/- 1296	383 +/- 518	839 +/- 1078	440 +/- 432	890 +/- 1080	751 +/- 572	1467 +/- 1678
O_3 (ppbv)	47 +/- 13	46 +/- 14	28 +/- 18	27 +/- 12	33 +/- 16	29 +/- 11	43 +/- 7	40 +/- 9

Carbon monoxide concentrations are relatively well simulated in all seasons with a small bias high in the Autumn and Winter. Ethane is underestimated in the spring and winter, but overestimates in the summer and autumn. Propane concentrations are

underestimated in all seasons. NO_y observations are in overestimate by the model, whereas NO and NO_2 concentrations are

220 underestimated.

The most visible model failure arises from the underestimate in the ethane and propane concentrations especially in the spring and winter. We therefore conduct a number of model experiments to investigate these observations. We first run simulations to assess the role of biomass burning in controlling the concentrations of these species at the site, we then assess how much the Asian anthropogenic source of these compounds would have to increase by, to give agreement between the model and the

225 measurements in the winter months.

4   Biomass burning sources

In order to understand the impact of biomass burning on the composition of the air arriving at the site we conduct additional simulation switching off the biomass burning emissions from North Asia and South Asia separately as shown in Figure 11. Two global simulations were run switching off the northern or southern biomass burning to generate new boundary conditions

230 and then these were used for the two regional simulations which again switched off the biomass burning in eirh the North or South of Asia.
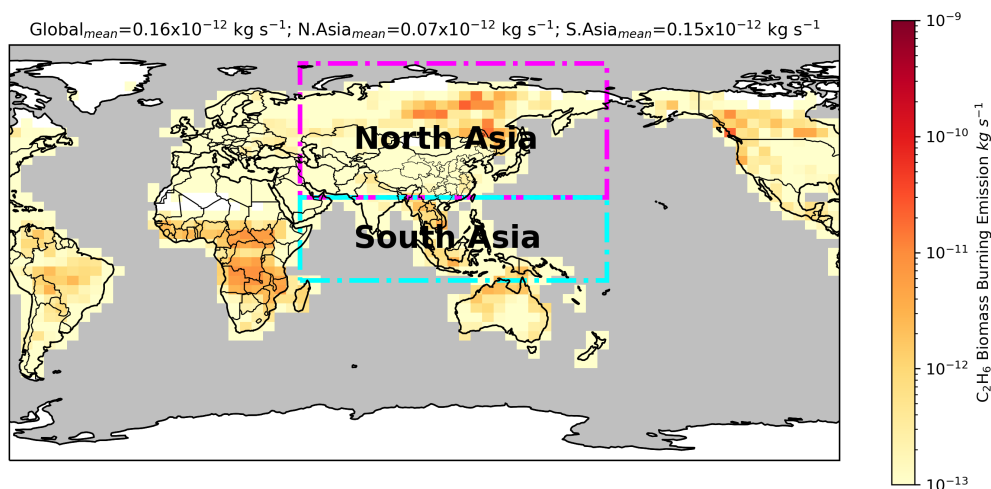
Figure 11. Annual mean biomass burning emission flux for C_2H_6 in 2018 (GFED). Regions indicated are the North and South Asia region which had biomass burning emissions switched off in the simulations

Figure 12 shows the time series of the percentage change in modelled concentrations of CO, O_3, C_2H_6 and C_3H_8 when biomass burning emissions in either the northern or southern domain are switched off. During the winter months the contributions are relatively small, however in the summer both sources can contribute significantly (20-35 %) to the modelled CO,

235 ethane and propane. The contributions are smaller for O_3 maximizing at 10 % during events in the summer time. These sharp

spikes correspond to the passing of typhoons in the area which can rapidly draw air from different direction for short period of time.
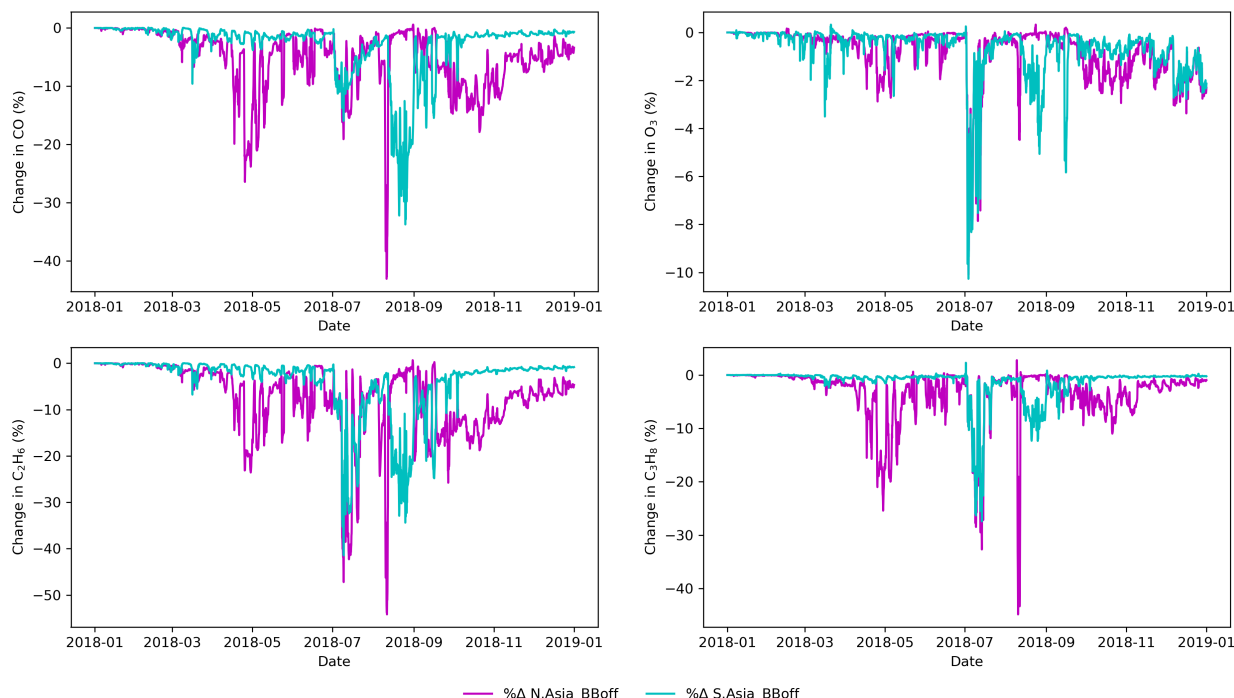
Figure 12. Percentage change in CO, O_3, C_2H_6 and C_3H_8 concentrations between standard and simulations without north Asian or south Asian biomass burning

The periods of model overestimate in summer ethane, notably in August (Figure 5), correspond to periods with a high fraction of modelled ethane biomass burning ($\sim$ 30%). However, the model overestimate (see Figure 5 is much large than this ($\sim$ 100 %). Thus, even if the biomass burning is switched off all together, the model over estimate would still remain. This suggests that the model overestimate is not primarily related to the modelled representation of biomass burning but likely results in uncertainties in the anthropogenic emissions of ethane south of Hateruma.

During the wintertime the model underestimates the observed ethane and propane. This is a period when the contribution from biomass burning is relatively low (<10%). Thus the potential for the underestimate in wintertime ethane and propane to be related to errors in the biomass burning appears to be small. Instead we now evaluate how much the Asian anthropogenic source of ethane and propane would have to be increased by, to fit the observed concentrations.

5 Anthropogenic emissions

The period between October to June (Figures 4 - 10) is characterised by elevated levels of pollution at the site from Russia, China, Korea and Japan (Figure 2). It is also a period when the model substantially underestimates the concentrations of ethane
250 and propane. In this section we explore what scaling factor would have to be applied to the Asian anthropogenic emissions of ethane and propane to better fit those observations.

Figure 13 (left) shows modelled ethane (top) and propane (bottom) plotted against observations in our base model. We separate the plot into summer (blue July-September) and winter (red October-June) period. It is obvious from the comparison that the winter time gradient is lower than expected (0.62 for ethane and 0.41 propane) whereas in the summer they are
255 substantially overestimate for ethane (3.97) and to a smaller extend so for propane (1.51).

Given the site's largest exposure to relatively recent north Asian emissions in the wintertime, we focus on this period and multiply the Asian anthropogenic emission of ethane and propane within the high-resolution domain by a first rough estimate of a correction factor "A" (1.75 for ethane and 2.58 for propane which are roughly 1./0.62 and 1./0.41) aimed at making the gradient of the best fit lines in the winter (S_w) to become 1. This would represent a correction factor if all of the ethane and
260 propane observed at the site were from within the simulation domain in Asia, and the oxidation lifetimes were correct.
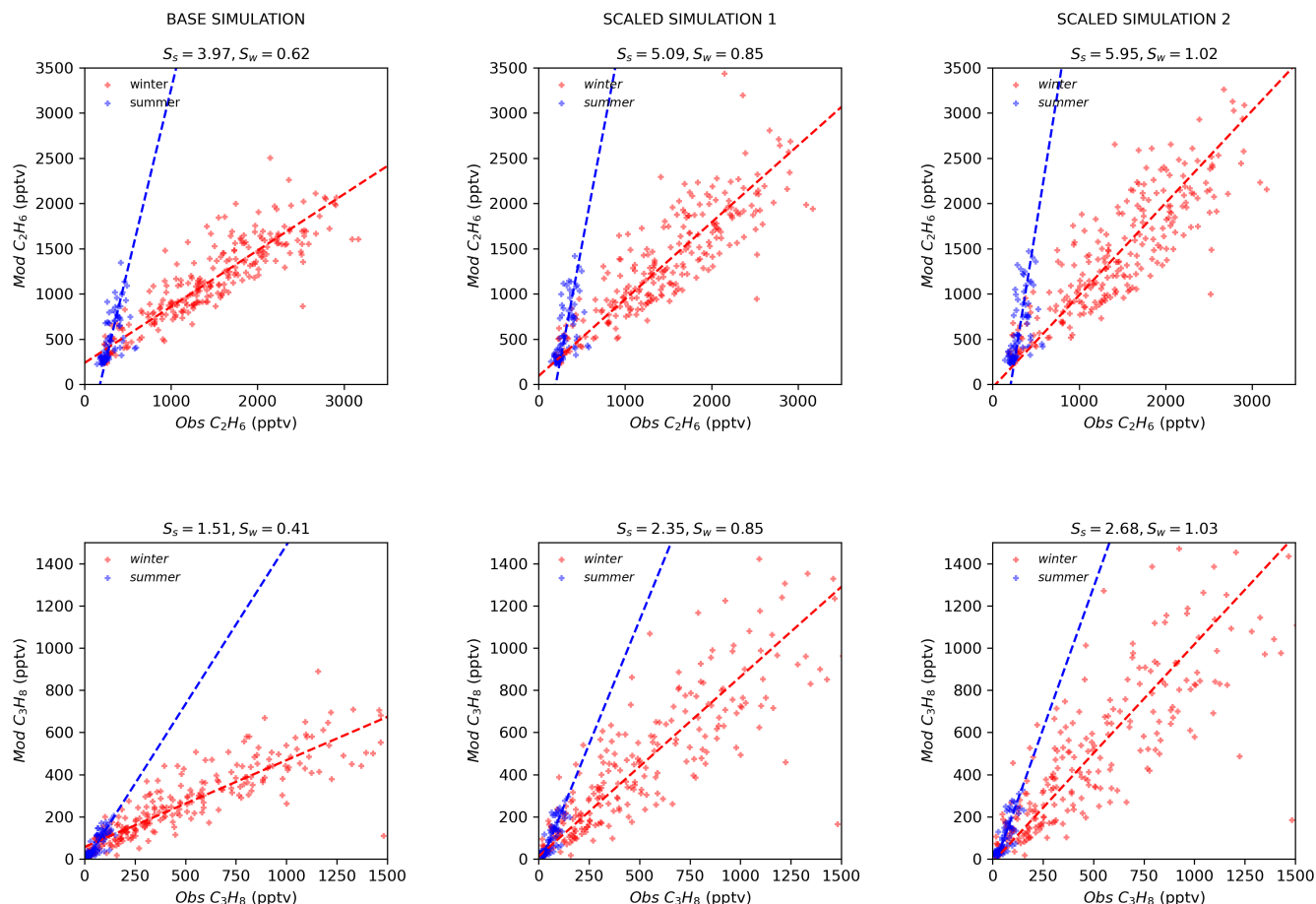
Figure 13. C_2H_6 and C_3H_8 modelled plotted against measurements in base simulation (left), scaled simulations with initial correction factor (middle) and optimized correction factor (right). Data is split into summer (July-September) in blue and winter (October-June) in red. S_s and S_w give the slope of the line of best fit for the timeseries in summer and winter respectively.

The annual simulation was re-run with the anthropogenic emissions of ethane and propane increased within the high resolution domain (Figure 13). From these two simulations (the base simulation and the simulation with an increased Asian emission within the domain of ethane and propane) allows the concentration of ethane and propane simulated at the site to be represented as $[X]=[X]_{Asian}+[X]_{background}$ in the base simulation; and $[X]=A \times [X]_{Asian}+[X]_{background}$ in the scaled simulation. Given the two equations, it is possible to solve the equations to find the value of A that gives the best performance between the measured and modelled species as indicated by the winter time gradient of best fit. This approach assumes a linear response between an increase in the emissions and the concentration, and that it doesn't have a significant impact on calculated OH concentrations.

265

The estimated optimal values of A are found to be 2.22 and 3.17 for ethane and propane respectively. This is also consistent
270 with the estimations using ratio of winter mean concentrations (calculated as 2.24 and 3.14 for ethane and propane respectively).
This gives ethane and propane measurement versus model scatter plot shown in Figures 13 (right) and 15, and a time series
shown in Figure 14.
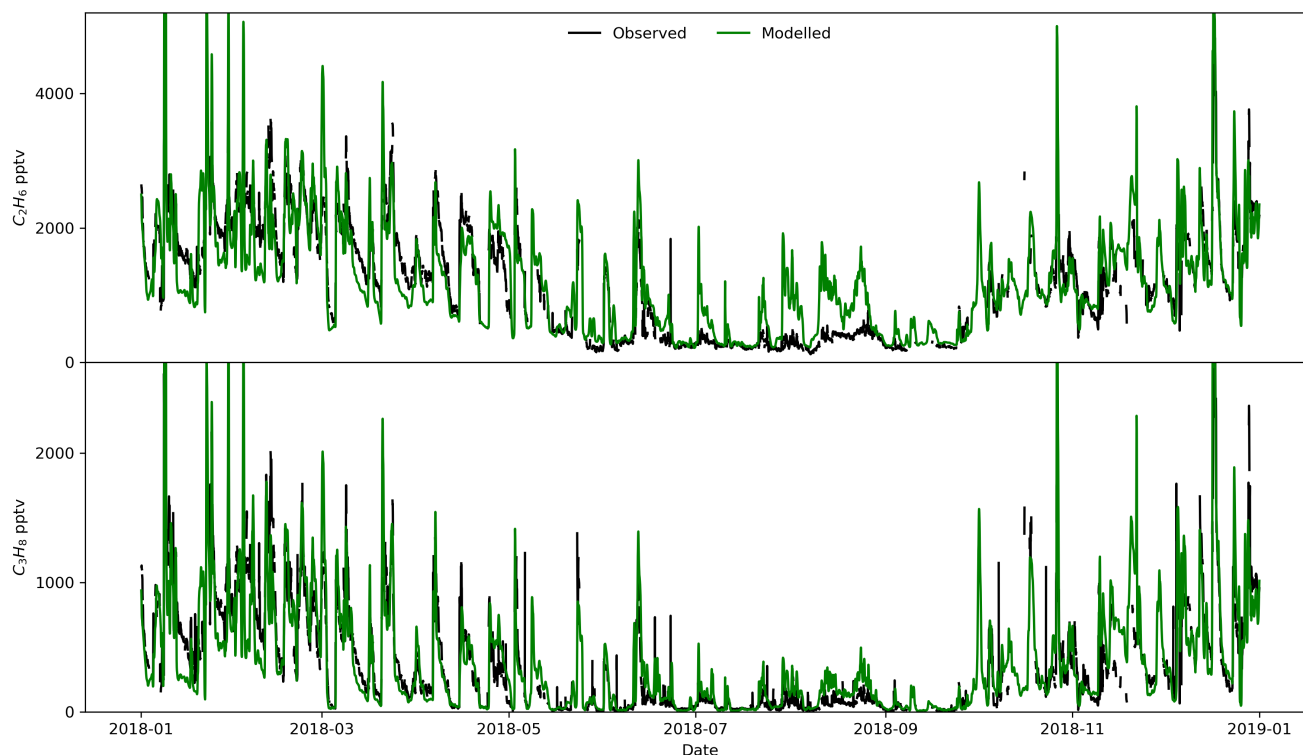
Figure 14. Timeseries of hourly C_2H_6 (top) and C_3H_8 (bottom) concentrations observed and with the static anthropogenic emissions.

For the winter months (October to June), when the air is predominantly off Northern Asia, the modelled ethane now has
a mean of 1443 +/- 737 (1σ) pptv, compared to observed mean was 1449 +/- 725 (1σ) pptv). The propane simulation has a
275 mean of 493 +/- 418 (1σ) pptv compared to am observed mean of 494 +/- 407 (1σ) pptv). During the summer months (July -
September), the model now significantly overestimates the ethane (mean simulated= 587 +/- 352 (1σ) pptv, mean observed=
308 +/- 99 (1σ) pptv) and propane (mean simulated = 105 +/- 88 (1σ) pptv, mean observed= 60 +/- 37 (1σ) pptv).
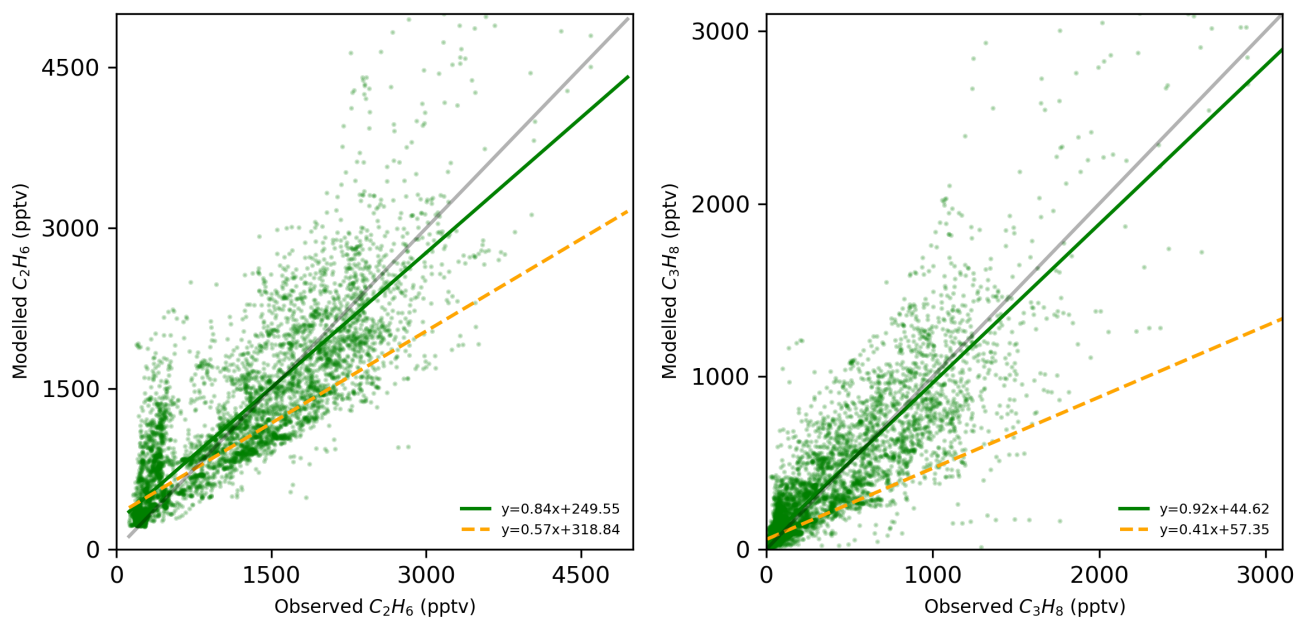
Figure 15. Scatter plot showing hourly C_2H_6 (left) and hourly C_3H_8 (right) concentrations between observation concentrations and model calculations with scaling (green). Yellow dashed line shows best fit line before scaling.

The wintertime improvement in model performance and the summertime degradation in performance, points towards a non-uniformity in the correction factor. This could indicate a difference in the seasonality of the emissions used here (a lower

280 increase in the summer than in the winter), or a different increase in north Asia which is primarily sampled from the site in the winter, to the south Asia which is primarily sampled in the summer.

Nonetheless, the observations here suggest a large increases in anthropogenic emissions of ethane and propane from north Asia. Large increases in global ethane and propane from those found in emissions inventories have been suggested before. Dalsøren et al. (2018) found it necessary to increase CEDS anthropogenic ethane emissions by a factor of roughly 2, and

285 CEDS propane emission by a factor of nearly 3 to get agreement between their model and observations. These are very similar to the conclusion found here. Tzompa-Sosa et al. (2017) found it necessary to substantially increase anthropogenic ethane source to fit observations. Mo et al. (2020) also measured vertical profiles of VOCs (including C_2H_6 and C_3H_8) and reported that emission fluxes were up to 3 times larger than in the Multi-resolution Emission Inventory for China (MEIC) inventory estimates. It seems likely that current estimates of north Asian emissions of ethane and propane are currently underestimated.

290 Figure 16 shows the impact of the large increase in Asian ethane and propane anthropogenic emissions on the concentrations of average hydroxyl radical and ozone in the region in July. The effect on the OH concentration in July was small and patchy with up to a 2% reduction in some places On the other hand, O_3 concentration increased slightly maximizing over Beijing where that amounts of a 2 % (around 1 ppbv) increase.
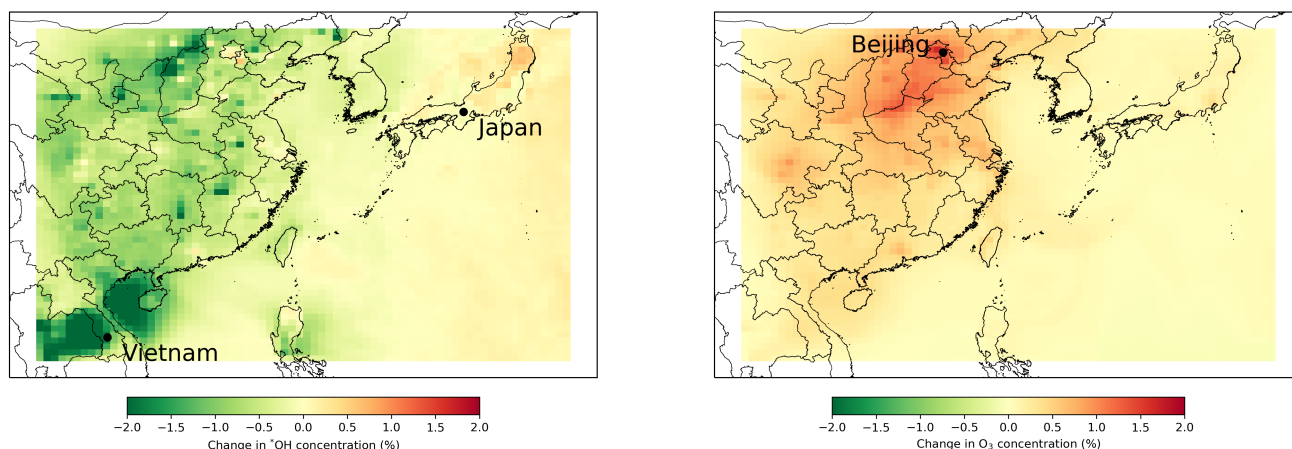
Figure 16. Percentage changes in July concentrations of OH (left) and O_3 (right) after increasing Asian ethane and propane anthropogenic emissions.

6 Conclusions

295   Measurement were made of a number of compounds in the air over the island of Hateruma (CO, C_2H_6, C_3H_8, NO, NO_2, NO_y and O_3). We show that the site mainly subject to clean Pacific air throughout the year. If the site is subjected to polluted air masses, these are more likely to have originated from north Asia (Russia, China, Japan, Korea etc) in the winter months and from south Asia (Philippines, Borneo and other regions in Southeast Asia including Vietnam, Indonesia, Peninsula Malaysia, Thailand) in the summer months. This gives the site a significant seasonal cycle in pollutant concentrations.

300   We have compared these observations to the output of the GEOS-Chem model, run in a regional configuration. We find that CO and O_3 are well simulated, the model overestimates NO_y observations, but tends to underestimates NO, NO_2, ethane and propane.

  We do not believe the overestimates in the NO_y can be attributed to problems with the simulation of shipping NO_x, as even switching off the shipping NO_x emissions doesn't remove the over estimate, but likely lies in the emissions of NO_x from 305 industrial regions close, issues with the chemistry or in the observations. The underestimates in ethane and propane during the winter period are unlikely to be reconciled by increases in biomass burning emissions, but could be reconciled by substantial (factors of 2 - 3) increases in the Asian anthropogenic source of these compounds (consistent with previous studies). These large increase in emissions have negligible influence on the hydroxyl radical concentrations and very little impact on the ozone in the region cities such as Beijing where there is up to 1 ppbv change in ozone concentration in July.

310   The site is located at an unusual location, which is subject to air masses from a large number of locations and so can be used to understand emissions of compounds from a number of location. Future plans to enhance the measurement capability at the site with a GC-MS system should allow an evaluation of a large number of different organic compounds, further enhancing the capacity to understand sources of pollution in the region.

Code and data availability. Hateruma data will be available from Global Environmental Database (https://db.cger.nies.go.jp/ged/en/index.html).

315 GEOS-Chem version 12.7.1 was used in this project DOI: 10.5281/zenodo.3676008 and input data files for GEOS-Chem can be downloaded from http://geoschemdata.wustl.edu

Appendix A: Comparison of simulation resolutions
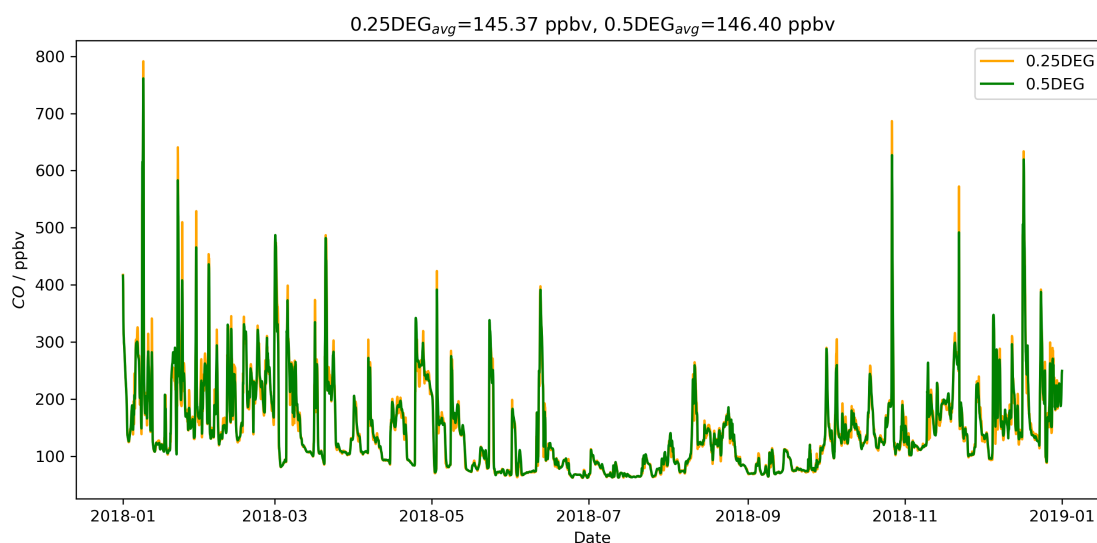
Figure A1. Modelled timeseries comparing CO simulation at $0.25° \times 0.3125°$ to $0.5° \times 0.625°$ resolution at the site
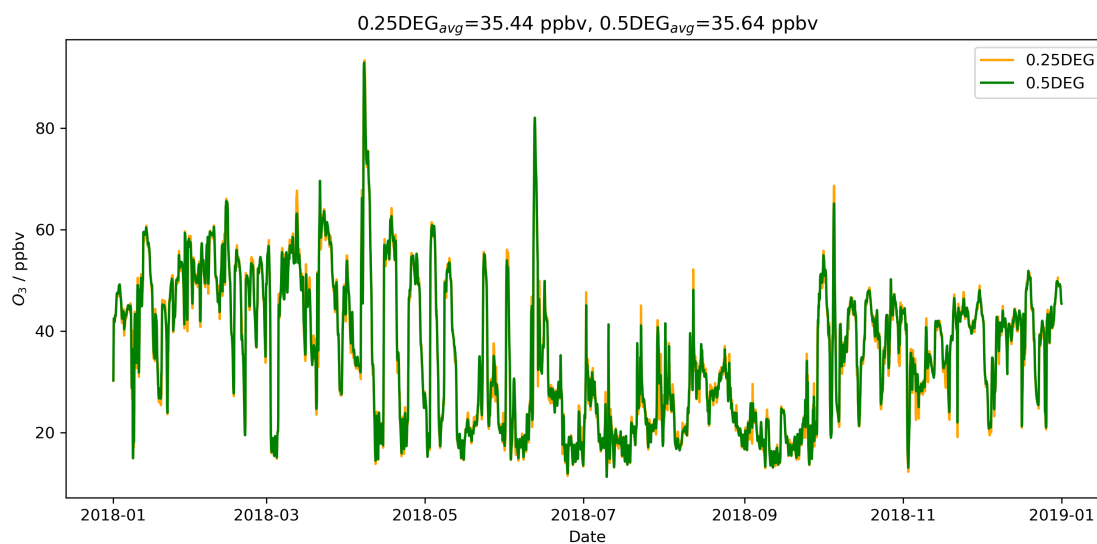
Figure A2. Modelled timeseries comparing O_3 simulation at $0.25° \times 0.3125°$ to $0.5° \times 0.625°$ resolution at the site
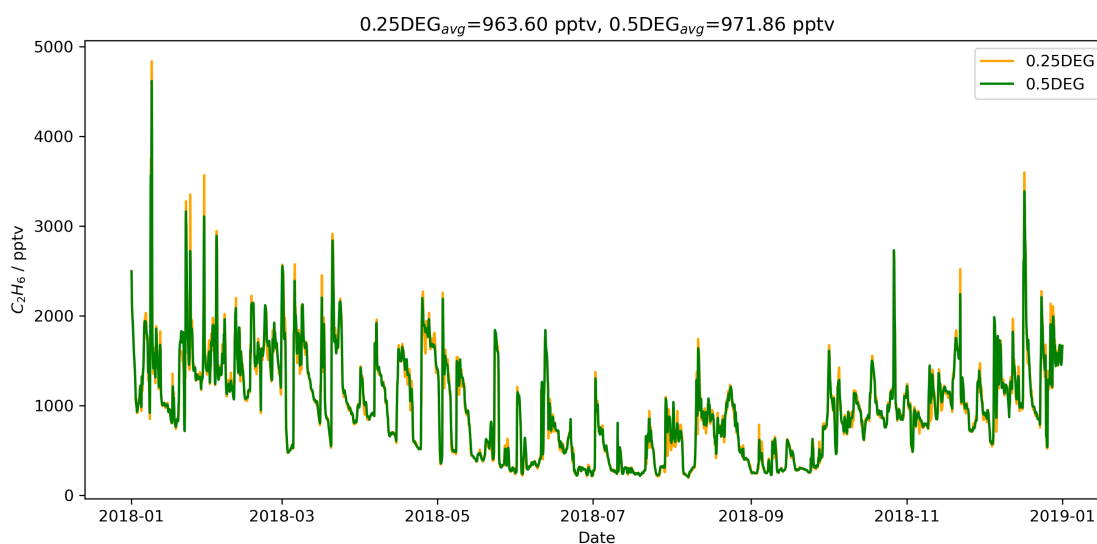
Figure A3. Modelled timeseries comparing C_2H_6 simulation at $0.25° \times 0.3125°$ to $0.5° \times 0.625°$ resolution at the site
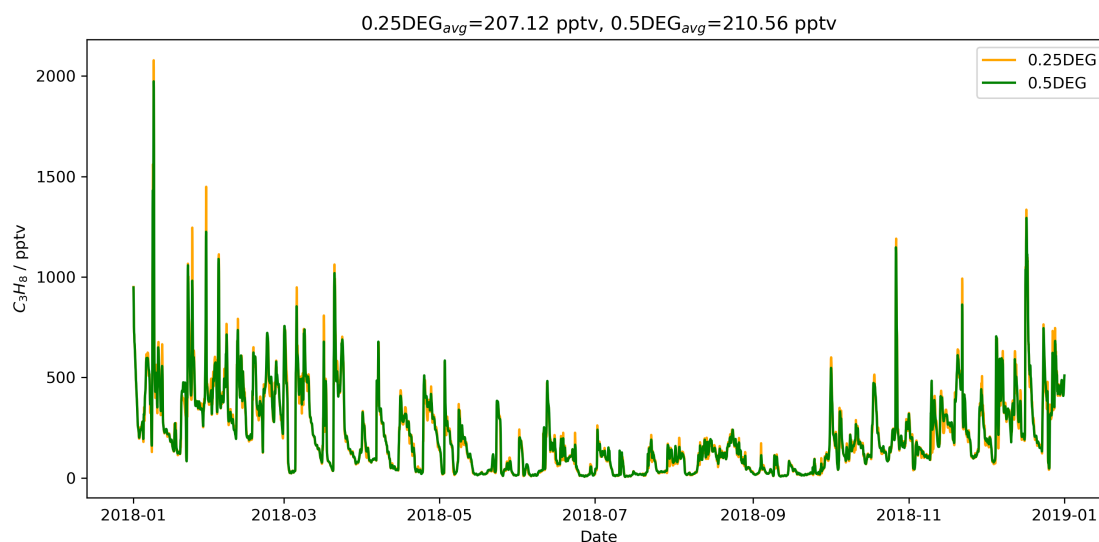
Figure A4. Modelled timeseries comparing C_3H_8 simulation at $0.25° \times 0.3125°$ to $0.5° \times 0.625°$ resolution at the site

Author contributions. AA ran the GEOS-Chem simulations and made the analysis and visualization of the model outputs. MR contributed the FLEXPART model outputs and visualization. ME, SA, AL, and TS developed the project. ME assisted in the analysis and interpretation

320 of all model outputs. TS provided the ethane and propane observations. YT contributed the CO data while SH, HM and HT provided the $NO/NO_2/NO_y$ and O_3 observations used in model validation. Paper was written by AA and ME with contributions from all co-authors

Competing interests. The authors declare that they have no conflict of interest

Acknowledgements. This project was undertaken on the Viking Cluster, which is a high performance compute facility provided by the University of York. We are grateful for computational support from the University of York High Performance Computing service, Viking and

325 the Research Computing team.

We would like to thank National Environment Research Council (NERC/UKRI) for providing support for this research through grant (Grant Reference: NE/S012273/1). We also thank National Centre for Atmospheric Science (NCAS) for their support.

This work was supported by JSPS under the National Centre for Atmospheric Science Joint Research Program implemented in association with UKRI (JRP-LEAD with UKRI). Grant number : [JSPSJRP20181708].

330 We thank staff members of the Global Environmental Forum Foundation (GEFF) for their great help in running the instruments at Hateruma station.

References

Akagi, S. K., Yokelson, R. J., Wiedinmyer, C., Alvarado, M. J., Reid, J. S., Karl, T., Crounse, J. D., and Wennberg, P. O.: Emission factors for open and domestic biomass burning for use in atmospheric models, Atmospheric Chemistry and Physics, 11, 4039–4072, https://doi.org/10.5194/acp-11-4039-2011, 2011.

Andreae, M. O. and Merlet, P.: Emission of trace gases and aerosols from biomass burning, Global Biogeochemical Cycles, 15, 955–966, https://doi.org/10.1029/2000GB001382, 2001.

Bey, I., Jacob, D. J., Yantosca, R. M., Logan, J. A., Field, B. D., Fiore, A. M., Li, Q., Liu, H. Y., Mickley, L. J., and Schultz, M. G.: Global modeling of tropospheric chemistry with assimilated meteorology: Model description and evaluation, Journal of Geophysical Research: Atmospheres, 106, 23 073–23 095, https://doi.org/10.1029/2001JD000807, 2001.

Carvalho, D., Rocha, A., Gómez-Gesteira, M., and Santos, C.: A sensitivity study of the WRF model in wind simulation for an area of high wind energy, Environmental Modelling Software, 33, 23–34, https://doi.org/10.1016/j.envsoft.2012.01.019, 2012.

Dalsøren, S. B., Myhre, G., Hodnebrog, Ø., Myhre, C. L., Stohl, A., Pisso, I., Schwietzke, S., Höglund-Isaksson, L., Helmig, D., Reimann, S., Sauvage, S., Schmidbauer, N., Read, K. A., Carpenter, L. J., Lewis, A. C., Punjabi, S., and Wallasch, M.: Discrepancy between simulated and observed ethane and propane levels explained by underestimated fossil emissions, 11, 178–184, https://doi.org/10.1038/s41561-018-0073-0, 2018.

Etiope, G., Ciotoli, G., Schwietzke, S., and Schoell, M.: Global geological CH_4 emission grid files, https://doi.org/10.25925/4J3F-HE27, 2018.

Etiope, G., Ciotoli, G., Schwietzke, S., and Schoell, M.: Gridded maps of geological methane emissions and their isotopic signature, Earth System Science Data, 11, 1–22, https://doi.org/10.5194/essd-11-1-2019, 2019.

Ferreira, A. P., Castanheira, J. M., Rocha, A., and Ferreira, J.: Estudo de sensibilidade das previsões de superfície em Portugal pelo WRF face à variação das parametrizações físicas, 2008.

Galbally, I.: Nitrogen oxides (NO, NO2, NOy) measurements at Cape Grim A technical manual, 2020.

Giglio, L., Randerson, J. T., and van der Werf, G. R.: Analysis of daily, monthly, and annual burned area using the fourth-generation global fire emissions database (GFED4), Journal of Geophysical Research: Biogeosciences, 118, 317–328, https://doi.org/10.1002/jgrg.20042, 2013.

Griffiths, P. T., Murray, L. T., Zeng, G., Shin, Y. M., Abraham, N. L., Archibald, A. T., Deushi, M., Emmons, L. K., Galbally, I. E., Hassler, B., Horowitz, L. W., Keeble, J., Liu, J., Moeini, O., Naik, V., O'Connor, F. M., Oshima, N., Tarasick, D., Tilmes, S., Turnock, S. T., Wild, O., Young, P. J., and Zanis, P.: Tropospheric ozone in CMIP6 simulations, Atmospheric Chemistry and Physics, 21, 4187–4218, https://doi.org/10.5194/acp-21-4187-2021, 2021.

Guenther, A. B., Jiang, X., Heald, C. L., Sakulyanontvittaya, T., Duhl, T., Emmons, L. K., and Wang, X.: The Model of Emissions of Gases and Aerosols from Nature version 2.1 (MEGAN2.1): an extended and updated framework for modeling biogenic emissions, Geoscientific Model Development, 5, 1471–1492, https://doi.org/10.5194/gmd-5-1471-2012, 2012.

Hoesly, R. M., Smith, S. J., Feng, L., Klimont, Z., Janssens-Maenhout, G., Pitkanen, T., Seibert, J. J., Vu, L., Andres, R. J., Bolt, R. M., Bond, T. C., Dawidowski, L., Kholod, N., Kurokawa, J.-I., Li, M., Lu, Z., Moura, M. C. P., O'Rourke, P. R., and Zhang, Q.: Historical (1750-2014) anthropogenic emissions of reactive gases and aerosols from the Community Emissions Data System (CEDS), Geoscientific Model Development, 11, 369–408, https://doi.org/10.5194/gmd-11-369-2018, 2018.

Holmes, C. D., Prather, M. J., and Vinken, G. C. M.: The climate impact of ship NO_x emissions: an improved estimate accounting for plume chemistry, Atmospheric Chemistry and Physics, 14, 6801–6812, https://doi.org/10.5194/acp-14-6801-2014, 2014.

Koike, M., Jones, N. B., Palmer, P. I., Matsui, H., Zhao, Y., Kondo, Y., Matsumi, Y., and Tanimoto, H.: Seasonal variation of carbon monoxide in northern Japan: Fourier transform IR measurements and source-labeled model calculations, Journal of Geophysical Research: Atmospheres, 111, https://doi.org/10.1029/2005JD006643, 2006.

Millet, D. B., Guenther, A., Siegel, D. A., Nelson, N. B., Singh, H. B., de Gouw, J. A., Warneke, C., Williams, J., Eerdekens, G., Sinha, V., Karl, T., Flocke, F., Apel, E., Riemer, D. D., Palmer, P. I., and Barkley, M.: Global atmospheric budget of acetaldehyde: 3-D model analysis and constraints from in-situ and satellite observations, Atmospheric Chemistry and Physics, 10, 3405–3425, https://doi.org/10.5194/acp-10-3405-2010, 2010.

Mo, Z., Huang, S., Yuan, B., Pei, C., Song, Q., Qi, J., Wang, M., Wang, B., Wang, C., Li, M., Zhang, Q., and Shao, M.: Deriving emission fluxes of volatile organic compounds from tower observation in the Pearl River Delta, China, Science of The Total Environment, 741, 139 763, https://doi.org/https://doi.org/10.1016/j.scitotenv.2020.139763, 2020.

Murray, L. T., Jacob, D. J., Logan, J. A., Hudman, R. C., and Koshak, W. J.: Optimized regional and interannual variability of lightning in a global chemical transport model constrained by LIS/OTD satellite data, Journal of Geophysical Research: Atmospheres, 117, https://doi.org/10.1029/2012JD017934, 2012.

National Centers for Environmental Prediction, National Weather Service, NOAA, U.S. Department of Commerce: NCEP GFS 0.25 Degree Global Forecast Grids Historical Archive, https://doi.org/10.5065/D65D8PWK, 2015.

Randerson, J. T., Chen, Y., van der Werf, G. R., Rogers, B. M., and Morton, D. C.: Global burned area and biomass burning emissions from small fires, Journal of Geophysical Research: Biogeosciences, 117, https://doi.org/10.1029/2012JG002128, 2012.

Reed, C., Evans, M. J., Di Carlo, P., Lee, J. D., and Carpenter, L. J.: Interferences in photolytic NO_2 measurements: explanation for an apparent missing oxidant?, Atmospheric Chemistry and Physics, 16, 4707–4724, https://doi.org/10.5194/acp-16-4707-2016, 2016.

Riddick, S.N.;Dragosits, U. T. F. S. M.: Global ammonia emissions from seabirds, https://doi.org/10.5285/c9e802b3-43c8-4b36-a3a3-8861d9da8ea9, 2012.

Saito, T., Yokouchi, Y., Stohl, A., Taguchi, S., and Mukai, H.: Large Emissions of Perfluorocarbons in East Asia Deduced from Continuous Atmospheric Measurements, Environmental Science & Technology, 44, 4089–4095, https://doi.org/10.1021/es1001488, pMID: 20441144, 2010.

Schlesinger, W. H. and Bernhardt, E. S.: Chapter 11 - The Global Carbon and Oxygen Cycles, in: Biogeochemistry (Fourth Edition), edited by Schlesinger, W. H. and Bernhardt, E. S., pp. 453–481, Academic Press, fourth edition edn., https://doi.org/10.1016/B978-0-12-814608-8.00011-6, 2020.

Sherwen, T., Schmidt, J. A., Evans, M. J., Carpenter, L. J., Großmann, K., Eastham, S. D., Jacob, D. J., Dix, B., Koenig, T. K., Sinreich, R., Ortega, I., Volkamer, R., Saiz-Lopez, A., Prados-Roman, C., Mahajan, A. S., and Ordóñez, C.: Global impacts of tropospheric halogens (Cl, Br, I) on oxidants and composition in GEOS-Chem, Atmospheric Chemistry and Physics, 16, 12 239–12 271, https://doi.org/10.5194/acp-16-12239-2016, 2016.

Shirai, T., Yokouchi, Y., Sugata, S., and Maksyutov, S.: HCFC-22 flux estimates over East Asia by inverse modeling from hourly observations at Hateruma monitoring station, Journal of Geophysical Research: Atmospheres, 115, 2010.

Stettler, M., Eastham, S., and Barrett, S.: Air quality and public health impacts of UK airports. Part I: Emissions, Atmospheric Environment, 45, 5415–5424, https://doi.org/10.1016/j.atmosenv.2011.07.012, 2011.

Stohl, A., Forster, C., Eckhardt, S., Spichtinger, N., Huntrieser, H., Heland, J., Schlager, H., Wilhelm, S., Arnold, F., and Cooper, O.: A backward modeling study of intercontinental pollution transport using aircraft measurements, Journal of Geophysical Research: Atmospheres, 108, https://doi.org/10.1029/2002JD002862, 2003.

Stohl, A., Forster, C., Frank, A., Seibert, P., and Wotawa, G.: Technical note: The Lagrangian particle dispersion model FLEXPART version 6.2, Atmospheric Chemistry and Physics, 5, 2461–2474, https://doi.org/10.5194/acp-5-2461-2005, 2005.

Tohjima, Y., Kubo, M., Minejima, C., Mukai, H., Tanimoto, H., Ganshin, A., Maksyutov, S., Katsumata, K., Machida, T., and Kita, K.: Temporal changes in the emissions of CH_4 and CO from China estimated from CH_4 / CO_2 and CO / CO_2 correlations observed at Hateruma Island, Atmospheric Chemistry and Physics, 14, 1663–1677, https://doi.org/10.5194/acp-14-1663-2014, 2014.

Tohjima, Y., Patra, P. K., Niwa, Y., Mukai, H., Sasakawa, M., and Machida, T.: Detection of fossil-fuel CO2 plummet in China due to COVID-19 by observation at Hateruma, 10, https://doi.org/10.1038/s41598-020-75763-6, 2020.

Tzompa-Sosa, Z. A., Mahieu, E., Franco, B., Keller, C. A., Turner, A. J., Helmig, D., Fried, A., Richter, D., Weibring, P., Walega, J., Yacovitch, T. I., Herndon, S. C., Blake, D. R., Hase, F., Hannigan, J. W., Conway, S., Strong, K., Schneider, M., and Fischer, E. V.: Revisiting global fossil fuel and biofuel emissions of ethane, Journal of Geophysical Research: Atmospheres, 122, 2493–2512, https://doi.org/10.1002/2016JD025767, 2017.

van der Werf, G. R., Randerson, J. T., Giglio, L., van Leeuwen, T. T., Chen, Y., Rogers, B. M., Mu, M., van Marle, M. J. E., Morton, D. C., Collatz, G. J., Yokelson, R. J., and Kasibhatla, P. S.: Global fire emissions estimates during 1997–2016, Earth System Science Data, 9, 697–720, https://doi.org/10.5194/essd-9-697-2017, 2017.

Weng, H., Lin, J., Martin, R., Millet, D. B., Jaeglé, L., Ridley, D., Keller, C., Li, C., Du, M., and Meng, J.: Global high-resolution emissions of soil NO x, sea salt aerosols, and biogenic volatile organic compounds, Scientific Data, 7, 1–15, https://doi.org/10.1038/s41597-020-0488-5, 2020.

Xiao, Y., Logan, J. A., Jacob, D. J., Hudman, R. C., Yantosca, R., and Blake, D. R.: Global budget of ethane and regional constraints on U.S. sources, Journal of Geophysical Research: Atmospheres, 113, https://doi.org/10.1029/2007JD009415, 2008.

Yokouchi, Y., Taguchi, S., Saito, T., Tohjima, Y., Tanimoto, H., and Mukai, H.: High frequency measurements of HFCs at a remote site in east Asia and their implications for Chinese emissions, Geophysical Research Letters, 33, https://doi.org/10.1029/2006GL026403, 2006.

Yokouchi, Y., Saito, T., Ooki, A., and Mukai, H.: Diurnal and seasonal variations of iodocarbons (CH_2ClI, CH_2I_2, CH_3I, and C_2H_5I) in the marine atmosphere, Journal of Geophysical Research: Atmospheres, 116, 2011.

Yokouchi, Y., Saito, T., Zeng, J., Mukai, H., and Montzka, S.: Seasonal variation of bromocarbons at Hateruma Island, Japan: implications for global sources, Journal of Atmospheric Chemistry, 74, 171–185, 2017.